

The Analyzer of Space Plasmas and Energetic Atoms (ASPERA-3) for the Mars Express Mission

S. Barabash, R. Lundin, H. Andersson, J. Gimholt¹, M. Holmström, O. Norberg², M. Yamauchi
Swedish Institute of Space Physics, Kiruna, Sweden

K. Asamura
Institute of Space and Astronautical Science, Sagami, Japan

A. J. Coates, D.R.Linder, D.O.Kataria,
Mullard Space Science Laboratory, University College London, UK

C. C. Curtis, K. C. Hsieh, B. R. Sandel
University of Arizona, Tucson, USA

A. Fedorov³, A. Grigoriev⁴, E. Budnik³,
Space Research Institute, Moscow, Russia

M. Grande, M. Carter, D. H. Reading
Rutherford Appleton Laboratory, Oxfordshire, UK

H. Koskinen, E. Kallio, P. Riihela, T. Säles,
Finnish Meteorological Institute, Helsinki, Finland

J. Kozyra
Space Physics Research Laboratory/University of Michigan, Ann Arbor, USA

N. Krupp, S. Livi⁵, J. Woch
Max-Planck-Institut für Aeronomie, Katlenburg-Lindau, Germany

J. Luhmann
Space Science Laboratory/University of California in Berkeley, Berkeley, USA

S. McKenna-Lawlor
Space technology Ltd., National University of Ireland, Ireland

S. Orsini, R. Cerulli-Irelli, A. Mura, A. Milillo
Istituto di Fisica dello Spazio Interplanetari, Rome, Italy

E. Roelof, D. Williams
Applied Physics Laboratory/John Hopkins University, Laurel, USA

J.-A. Sauvaud, J.-J. Thocaven
Centre d'Etude Spatiale des Rayonnements, Toulouse, France

D. Winningham, R. Frahm, J. Scherrer, J. Sharber
Southwest Research Institute, San Antonio

P. Wurz, P. Bochsler,
University of Bern, Physikalisches Institut, Switzerland

¹ Now at Scania, Volvo Corporation, Södertälje, Sweden

² Now at ESRANGE, Swedish Space Corporation, Kiruna, Sweden

³ Now at Centre d'Etude Spatiale des Rayonnements, Toulouse, France

⁴ Now at Swedish Institute of Space Physics, Kiruna, Sweden

⁵ Now at Applied Physics Laboratory/John Hopkins University, Laurel, USA

Abstract. The general scientific objective of the ASPERA-3 experiment is to study the solar wind - atmosphere interaction and characterize the plasma and neutral gas environment in the near-Mars space through energetic neutral atom (ENA) imaging and local charged particle measurements. The studies to be performed address the fundamental question: How strongly do the interplanetary plasma and electromagnetic fields affect the Martian atmosphere? This question is directly related to the problem of Martian dehydration. The ASPERA-3 instrument comprises four sensors; two ENA sensors, electron and ion spectrometers. The Neutral Particle Imager (NPI) provides measurements of the integral ENA flux (0.1 – 60 keV) with no mass and energy resolution but high angular resolution.

The Neutral Particle Detector (NPD) provides measurements of the ENA flux, resolving velocity (0.1 – 10 keV) and mass (H and O) with a coarse angular resolution. The electron spectrometer (ELS) is a standard top-hat electrostatic analyzer in a very compact design. These three sensors are located on a scanning platform providing a 4 coverage (maximum possible). The instrument also contains an ion mass composition sensor, IMA (Ion Mass Analyzer). Mechanically, IMA is a separate unit connected by a cable to the ASPERA-3 main unit. IMA provides ion measurements in the energy range 0.01 - 40 keV/q for the main ion components H^+ , H_2^+ , He^+ , O^+ , with 20-80 amu/q.

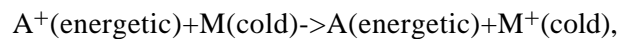
1. THE SCIENCE

1.1. Scientific Task

The scientific objectives of the Mars Express Orbiter mission are to study the subsurface, the surface, and the atmosphere of Mars, as well as the interaction of the atmosphere with the interplanetary medium. The experiment ASPERA-3 (Analyzer of Space Plasma and Energetic Atoms) will fulfill the last scientific objective carrying out:

- remote measurements of energetic neutral atoms (ENA) in order to (a) investigate the interaction between the solar wind and Martian atmosphere, (b) characterize quantitatively the impact of plasma processes on the atmospheric evolution, and (c) obtain the global plasma and neutral gas distributions in the near - Mars environment,
- *in situ* measurements of ions and electrons in order to (a) complement the ENA images (electrons and multiply-charged ions cannot be imaged) (b) to study local characteristics of plasma (dynamics and fine structure of boundaries) (c) provide undisturbed solar wind parameters necessary for interpretation of ENA images.

As was established by earlier missions, and confirmed recently by the Mars Global Surveyor, Mars does not possess an intrinsic dipole magnetic field but only local crustal magnetizations [Acuna *et al.*, 1998]. The local field plays a role in the solar wind interaction only over limited regions, while for the overall interaction picture, the solar wind interacts directly with the Martian ionosphere, exosphere, and upper atmosphere. As a result of the low gravity on Mars, the neutral density can reach $10^4 - 10^6 \text{ cm}^{-3}$ in the interaction region where the main plasma boundaries, the bow shock and the magnetopause are located. The co-existence of these two components, the solar wind plasma and the planetary neutral gas, results in a strong interaction between them. One of the fundamental collisional interactions is the charge - exchange process between the energetic ion, A^+ , and the cold atmospheric gas, M:



that produces energetic neutral atoms, A, and an ionized gas particle. Directional detection of the ENA thereby yields a global image of the interaction, if the observer is at a remote location with respect to the plasma population [Wurz, 2000]. The ASPERA-3 experiment will concentrate on studying the effects of the plasma - neutral coupling at Mars via ENA imaging, complemented by the electron and ion observations.

1.2 The Solar Wind - Atmosphere Coupling

Near-Mars space is strikingly different from Earth-space because of the absence of a substantial intrinsic magnetic field of Mars. Without the magnetic cavity of a magnetosphere to shield the upper atmosphere from the on-coming solar wind, Mars is subject to comet-like atmosphere erosion processes and solar-wind-induced current systems that have no terrestrial counterparts. From previous missions to Mars (especially the Phobos-2 mission) and experience gained in orbit around similarly weakly magnetized Venus on the Pioneer Venus Orbiter, we have developed ideas of how the Mars upper atmosphere and solar wind interact and the consequences for the planet. In particular, we have observed that the scavenging of planetary ions may have resulted in the removal of ~1 m of surface water over 4.5 billion years [Lundin *et al.*, 1991]. More detailed studies [Perez-de-Tejada, 1992], that take into account the variability of the ionosphere throughout the planetary history, give a much higher (~30 m) equivalent depth of water, that has escaped due to the solar wind interaction process.

The current atmospheric conditions on Mars indicate that water does not exist on the surface in any significant amount (an equivalent water layer is 15 μm deep [Farmer *et al.*, 1977]). On the other hand, independent analyses of several features of the planet unambiguously indicate that water did exist in the past on the Martian surface. Figure 1 shows the water inventory based on different

approaches, namely, geomorphologic features, analysis of the SNC meteorites, isotopic abundance and volcanic activity (Figure was adopted from the review by *McKay and Stoker* [1989]). The total amount of water that existed in the past on the surface resulted in an equivalent water layer of 100 m, at least. Thus we come to the problem of Mars dehydration. Where is the Martian water? Is it lost or frozen and buried? If it is the former, what could produce such an effective escape mechanism? If the latter, where is this tremendous amount of water stored? As indicated above, the processes associated with the solar-wind interaction could account for the escape of up to 30% the amount of water present on the surface in the past.

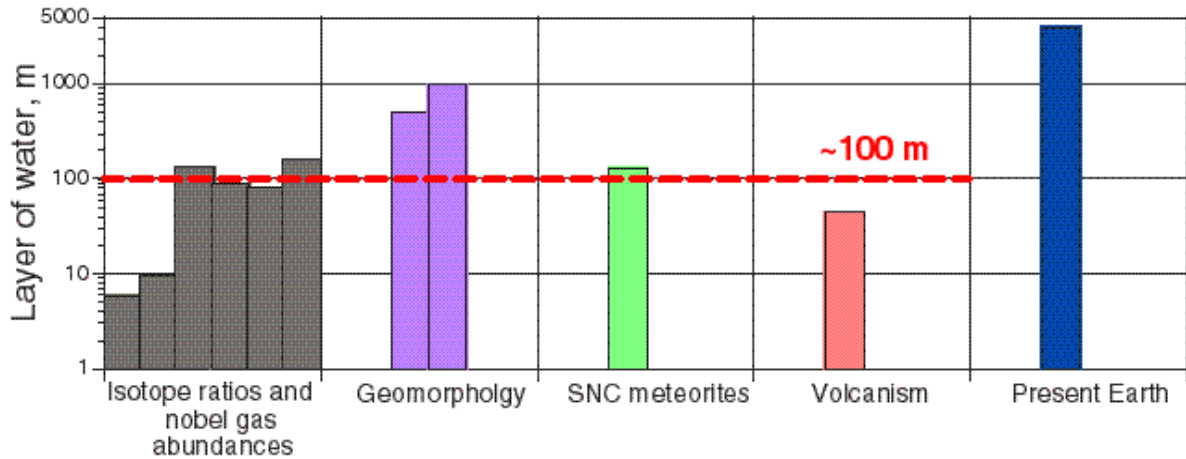


Figure 1. Martian water inventory based on different approaches. The present Earth is also shown for reference (adopted from *McKay and Stoker* [1989]).

Another problem of the solar wind - atmosphere coupling that has not been explored experimentally concerns the energetic consequences for the Martian atmosphere of the lack of a Martian dipole field of any importance. Kinetic and test-particle models of the Mars-solar wind interaction [*Brecht*, 1997; *Kallio et al.*, 1997] suggest that solar wind absorption by the Martian atmosphere may be an important energy source for the upper atmosphere. The ENAs generated as a product of the solar - wind interaction further enhance the deposition of solar wind energy [*Kallio and Barabash*, 2000b] and, at the same time, provide a means of "imaging" the solar wind interaction. The Martian atmosphere, although thin, alters the incoming energetic solar wind by (a) generation of ionospheric currents that partially deflect the ion flow around the Martian ionosphere, (b) "mass loading" the solar wind with planetary ions produced mainly by photoionization, and solar wind electron impact ionization of the atmospheric gases, and (c) undergoing charge-transfer or charge-exchange interactions with the solar wind ions. According to the models, some of the solar wind ions (mainly protons and alphas) directly impact Mars' upper atmosphere near its exobase (at ~180 km altitude) because their gyroradii are too large to behave as a deflected "fluid" in the subsolar magnetosheath (see *Brecht* [1997] and *Kallio and Janhunen* [2001]) or because they are partially thermalized by the bow shock [*Kallio et al.*, 1997]. Others undergo charge exchange reactions with ambient exospheric and thermospheric neutrals, particularly hydrogen and helium and then impact the exobase as ENAs [*Kallio et al.*, 1997]. In both cases, solar wind energy is "directly" deposited into the upper atmosphere resulting in increasing ionization rates and UV emissions. *Kallio and Barabash* [2000, 2001] have studied the effects of such ENA precipitation using Monte Carlo simulations and estimated that under the typical solar wind conditions the precipitating hydrogen atoms increase the ionization rate by about 1% in comparison with ionization rates due to extreme ultraviolet radiation. This effect is comparable, or even stronger, than similar effects caused by the O^+ and H^+ precipitation [*Luhmann and Kozyra*, 1991; *Brecht*, 1997; *Kallio and Janhunen*, 2001]. The results also indicate that a substantial part of the incoming particles is scattered back from the Martian atmosphere resulting in an ENA hydrogen albedo. Imaging these particles would visualize the spots or regions of the most intense ENA precipitation.

While the energy transfer associated with the proton or ENA precipitation exceeds the one from the O^+ precipitation, it is the oxygen ions that causes massive sputtering of the atmosphere [*Luhmann and Kozyra*, 1991; *Luhmann et al.*, 1992]. *Luhmann and Bauer* [1992] estimated that the O^+ sputtering results in the escape of 0.1 – 0.5 kg/s of oxygen atoms. That is on the same level as the

non-thermal escape of the hot oxygen atmospheric component. For comparison, the direct solar wind pick – up, not including the bulk ionospheric scavenging, removes 0.01 kg/s at most.

1.3 Sources of Energetic Neutral Atoms at Mars

Barabash et al. [1995a], *Kallio et al.* [1997], *Holmström et al.* [2001], *Mura et al.*, [2001], *Lichtenegger et al.*, [2001], *Barabash et al.* [2001] considered the ENA production at Mars. ENAs are produced by charge - exchange between the Martian exosphere containing H, H₂, He and O, and the different plasma populations such as (1) the supersonic solar wind [*Holmström et al.*, 2001], (2) the shocked solar wind [*Holmström et al.*, 2001], and (3) accelerated planetary ions [*Barabash et al.*, 2001; *Lichtenegger et al.*, 2001]. The tiny Phobos atmosphere (4) can also interact with both the supersonic and the shocked solar wind resulting in ENA generation [*Mura et al.*, 2001]. The energetic O⁺ ions picked up by the plasma flow incident on the atmosphere sputter or backscatter oxygen, CO₂ and its fragments [*Luhmann and Kozyra*, 1991; *Luhmann et al.*, 1992]. The back-scattered atoms have energies up to few hundred eV and form an oxygen ENA albedo (5). The intensity of these emissions directly determines the efficiency of the atmospheric erosion. The precipitating protons and hydrogen ENAs can also be scattered back forming a hydrogen ENA albedo (6) [*Kallio and Barabash*, 2001; *Holmström et al.*, 2001]. With the ASPERA-3 experiment we are going to study all these six ENA sources.

The supersonic solar wind upstream of the bow shock can experience charge - exchange with the Martian hydrogen exosphere over very long distances resulting in a narrow ($\sim 10^\circ$) anti-sunward beam of ENAs with the energy of the bulk flow of the solar wind (the spectrum marked by arrows in Figure 2). Detection of these ENAs can be made only at the beam edges because it is superimposed on the intense flux of the solar radiation.

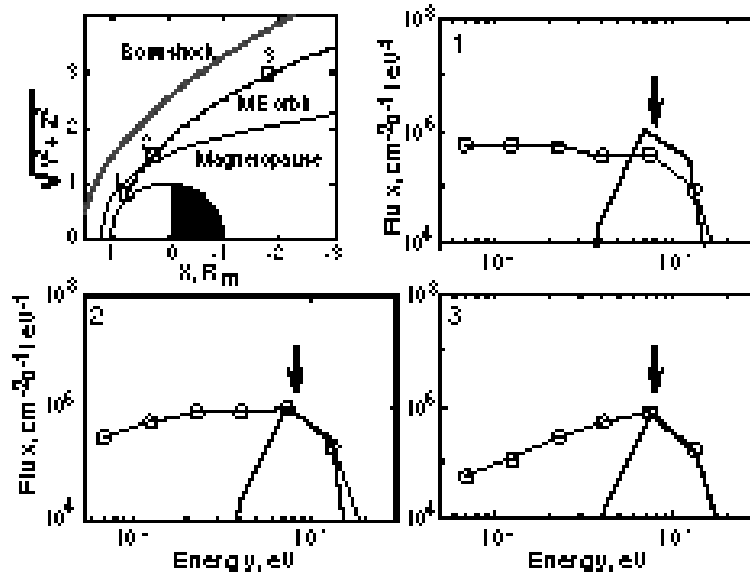


Figure 2. ENA spectra along the Mars Express orbit. The ENAs originate in the shocked solar wind. The arrows mark ENA flux produced in the upstream solar wind. The energy resolution corresponds to that for ASPERA-3.

The shocked solar wind is the strongest source of ENAs since the protons flowing around the Martian obstacle can interact with dense neutral gas. The detailed modeling of the ENA production from this source was performed by *Kallio et al.* [1997], *Holmström et al.*, [2001], and *Mura et al.*, [2001]. Using these models we simulate ENA images that would be observed from the Mars Express orbit for the solar maximum conditions. The spacecraft will actually reach Mars during the moderate solar activity characteristic of the decline of the solar cycle, but the ENA emissions are weaker during the solar maximum and our calculations give, thus, the lower limits for the ENA fluxes. Figure 2 shows the ENA spectra integrated over the unit sphere for several locations along the Mars Express orbit. The estimated ENA fluxes are well above $10^4 \text{ cm}^{-2} \text{ s}^{-1} \text{ keV}^{-1}$ and therefore easily detectable. The directional fluxes to be measured well exceed $10^5 \text{ cm}^{-2} \text{ s}^{-1} \text{ sr}^{-1}$.

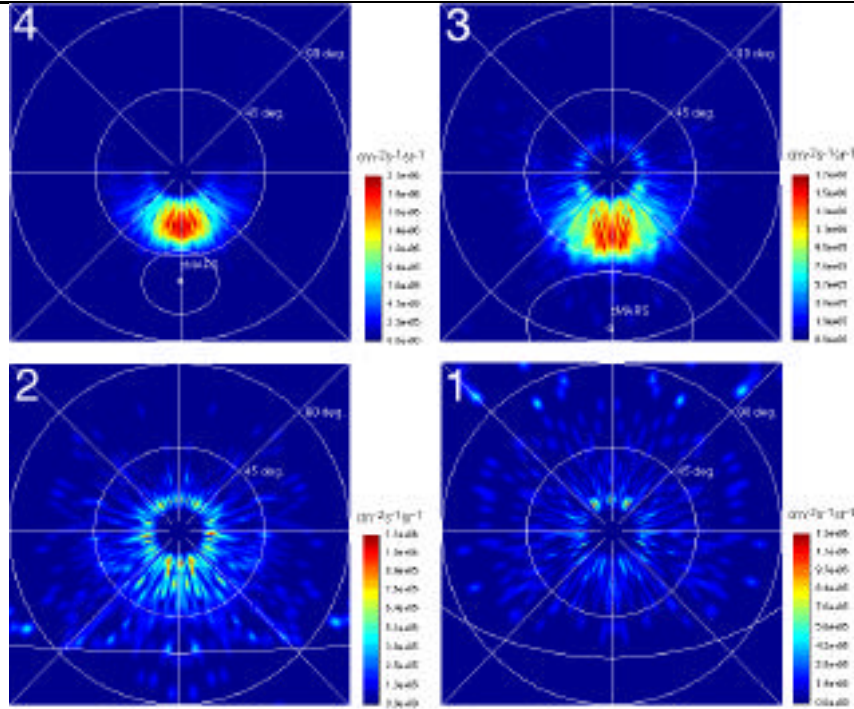


Figure 3. ENA images for four locations along the Mars Express orbit marked in the inset of Figure 2. The position 4 not shown in Figure 2 corresponds to the orbit apocenter. The polar axis is looking toward the Sun. The polar angle is the azimuth at the vantage point and the radius the polar angle to the Sun direction. The solar wind ENAs are blocked.

Figure 3 shows the directional ENA flux integrated over energy as a function of two spherical angles (ENA images) for several positions along the Mars Express orbit marked in Figure 2. Position 4 corresponds to the apocenter. In this fish-eye projection, the polar axis is looking toward the Sun. The polar angle is the azimuth at the vantage point and the radius the polar angle to the Sun direction. The images display the entire interaction region and can be converted into global distributions of the proton flow and neutral gas using extracting diagnostic methods similar to the one developed for the Earth's conditions [Roelof and Scinner, 2000]. Holmström *et al.*, [2001] showed that the ENA fluxes generated from the shocked solar wind are most sensitive to the neutral hydrogen distribution controlled by the exobase temperature and the position of the boundary separating the solar wind and planetary plasmas.

Some of the ENAs produced by the shocked solar wind as well as ENAs originating in the solar wind can precipitate onto the Martian ionosphere. Figure 2 (position 1 inside the magnetosphere) gives a typical spectrum of precipitating ENAs at the 45° solar zenith angle. The spectrum is rather flat at the level $7 \cdot 10^5 \text{ cm}^{-2} \text{ s}^{-1} \text{ keV}^{-1}$. The peak corresponds to the solar wind energy. The planetary protons originating from ionization of the hydrogen corona can charge - exchange with the exospheric gas as well, resulting in planetary hydrogen ENA emissions. These emissions investigated in detail by Lichtenegger *et al.* [2000] differ from the shocked solar wind ENAs in energy because the pick-up protons can gain an energy up to four times the solar wind energy.

The ASPERA/PHOBOS observations of the plasma energization inside the Martian magnetosphere [Lundin *et al.*, 1993] have shown the existence of two basic ion populations, the tail beams of H^+ and O^+ with energy 1-3 keV and outflowing ionospheric ions with energy 10 - 100 eV near the tail flanks. Barabash *et al.* [1995a] estimated the related ENA flux to be $10^3 \text{ cm}^{-2} \text{ s}^{-1} \text{ keV}^{-1}$ for the energy range 1 - 10 keV, and up to $10^5 \text{ cm}^{-2} \text{ s}^{-1} \text{ keV}^{-1}$ for the lower energies 10 - 100 eV. The ENA signal associated with the pick-up oxygen was investigated in detail by Barabash *et al.* [2001]. Using the empirical model of the solar wind plasma flow near Mars developed by Kallio and Koskinen [1999], Barabash *et al.* [2001] solved numerically the kinetic equation and obtain the global distribution of oxygen ions. This distribution is then converted to the corresponding ENA flux. It was found that the fluxes of the oxygen ENAs could reach $10^4 \text{ cm}^{-2} \text{ s}^{-1} \text{ sr}^{-1} \text{ eV}^{-1}$ and fully reflect the morphology of the oxygen population. This provides a way to determine the instantaneous oxygen escape rate. One of the simulated images for the energy range 0.1 – 1.65 keV is reproduced in Figure 4. The projection

is similar to the one used for hydrogen ENA images but the polar axis in the vantage point points towards the center of the planet. The image shows a strong jet of ENA coming out from the subsolar point where the electric and magnetic field configuration effectively accelerates newborn planetary ions. The tailward flow is also clearly reproduced. The corresponding vantage points are shown below the images.

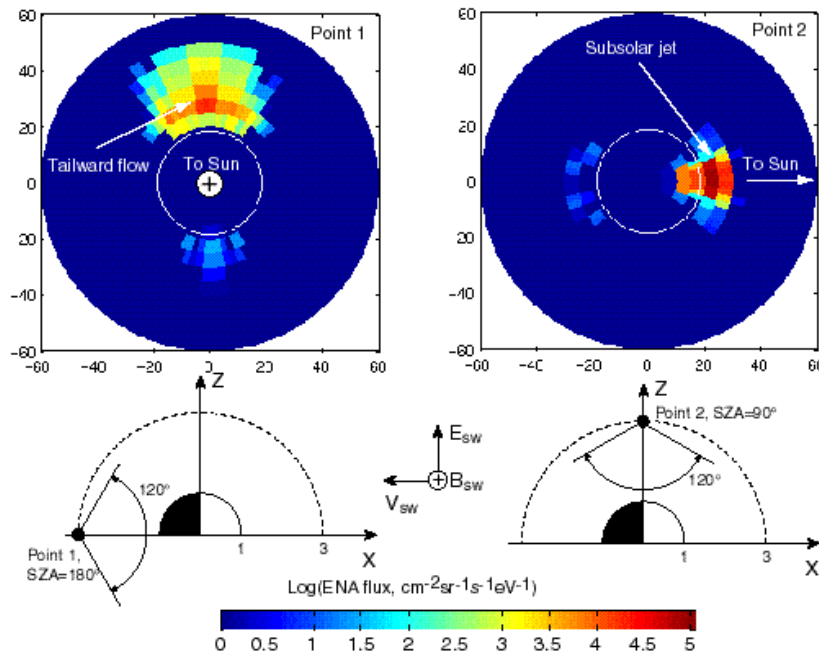


Figure 4. ENA images of the pick-up oxygen ions for two vantage points in the tail and at the pole. The vantage points are in the plane perpendicular to the ecliptic. The polar axis is towards the planetary center. The image projection is similar to the one on Fig. 3. The energy range is 0.1 – 1.65 keV. The electric and magnetic field vectors in the solar wind are also shown for reference.

Several experiments on the PHOBOS mission observed brief plasma disturbances when the spacecraft crossed the Phobos orbit (see review and references by *Barabash* [1995b]). They could be related to a hypothetical neutral gas torus resulting from the moon outgassing. The solar wind plasma can experience charge - exchange with the Phobos "atmosphere" and the neutral torus resulting in ENA emissions. Assuming an outgassing rate of 10^{23} s^{-1} *Mura et al.* [2001] calculated the associated ENA flux on the order of $10^3 - 10^4 \text{ cm}^{-2}\text{s}^{-1}\text{keV}^{-1}$ for the shocked solar wind plasma and up to $10^6 \text{ cm}^{-2}\text{s}^{-1}\text{keV}^{-1}$ for the solar wind beam. Due to solar radiation, the Phobos ENAs and the Phobos torus ENAs can only be observed when the moon is in the magnetosheath and the plasma flow deviates strongly from the anti-solar direction.

1.4 ENA Imaging of the Martian Environment

With the ASPERA-3 experiment we image all of the above ENA sources. ENA images to be obtained provide twofold information. First of all, they reveal morphological features of the ENA sources such as the location of boundaries and their relative sizes. ENA images are useful, in particular, for investigating different types of asymmetries expected for the plasma flow near Mars [*Dubin et al.*, 1996].

The ENA images of the escaping plasma display globally and instantaneously the size and geometry of the outflowing plasma region. These characteristics are particularly important for calculations of the total non-thermal plasma outflow. For instance, the local ion measurements made using two instruments, ASPERA and TAUS, during the PHOBOS mission gave comparable ion fluxes. However, different assumptions made regarding the outflow region geometry (mass - loading boundary, plasma sheet) resulted in significant differences in the total outflow rate estimations, 0.5 - 1.0 kg/s [*Lundin et al.*, 1989] and 0.15 kg/s [*Verigin et al.*, 1991]. One of the reasons for this was ambiguity in separating spatial and temporal variations, which is typical for local plasma measurements. Global and instantaneous observations of the outflowing plasma region morphology

to be made via ENA imaging would help to resolve this issue which is important for understanding the planetary atmosphere evolution.

Beside morphological features, ENA images carry an ample amount of quantitative information about both the planetary plasma and neutral environments. By applying the extraction techniques to the images of the shocked solar wind, we plan to obtain the quantitative models giving the neutral gas profiles, namely, the exobase densities and temperatures, and global proton plasma distributions, namely, the flow geometry, bulk velocity, density, and temperature.

Recent aerobraking measurements from the Mars Global Surveyor (*Dornheim, 1997*) indicate that the atmospheric density at 150 km altitude varies by 30% in one out of three passes. Estimated scale heights of ~8 km implies that the densities in the interaction region higher up will also be much more variable with time than had been expected. Global ENA imaging of the interaction offers the greatest promise of separating the spatial and temporal variations of the atmosphere - solar wind interaction. Apart from imaging, the measurements of ENA flux from certain directions provide a diagnostic tool for plasma - atmosphere coupling studies. Precipitating ENAs and ENA albedo (back-scattered oxygen) are direct manifestation of such an interaction.

1.5 Scientific Objectives and Measurements Requirements

The studies of Martian ENAs resulting from the solar wind - atmosphere interaction address the fundamental question: *How strongly do the interplanetary plasma and electromagnetic fields affect the Martian atmosphere?* This question is directly related to the problem of Martian dehydration as described in Section 1.2. *What happened to the Martian water* that once flowed in numerous channels? As we know from our Earth's experience, together with an inventory of organic compounds and external energy sources, liquid water is a fundamental requirement for life as we know it. Therefore, a clear understanding of the fate of the Martian water is a crucial issue in resolving the *problem whether or not life existed on Mars in the past.*

The general scientific task, to study the solar wind - atmosphere interaction through ENA imaging, can be subdivided into specific scientific objectives, these are listed in Table 1 together with the corresponding instrument requirements.

Table 1. The ASPERA-3 scientific objectives

Scientific objectives	Associated measurements	Measurement requirements
Determine the instantaneous global distributions of plasma and neutral gas near the planet	ENAs originating from the shocked solar wind	Measure the ENA flux in the energy range tens eV - few keV with 4 coverage. ENA flux $> 10^4 \text{ cm}^{-2}\text{s}^{-1}\text{keV}^{-1}$ Measure the upstream solar wind parameters
Study plasma induced atmospheric escape	ENAs originating from the inside of the magnetosphere	Mass resolving (H / O) ENA measurements in the energy range up to tens keV. ENA flux $> 10^3 \text{ cm}^{-2}\text{s}^{-1}\text{keV}^{-1}$
Investigate the modification of the atmosphere through ion bombardment	ENA albedo	Mass resolving (H / O) ENA measurements in the energy range down to tens eV from the nadir direction ENA flux $> 10^6 \text{ cm}^{-2}\text{s}^{-1}\text{keV}^{-1}$ (100 eV)
Investigate the energy deposition from the solar wind to the ionosphere	Precipitating ENAs	ENA measurements in the energy range tens eV - few keV. ENA flux $> 10^4 \text{ cm}^{-2}\text{s}^{-1}\text{keV}^{-1}$
Search for the solar wind - Phobos interactions	ENA originating from Phobos	ENA measurements in the energy range tens eV - few keV with 4 coverage ENA flux $10^4 \text{ cm}^{-2}\text{s}^{-1}\text{keV}^{-1}$
Define the local characteristics of the main plasma regions	Ions and electron measurements of hot plasma	Ion and electron measurements in the energy range few eV - tens keV with 4 coverage

1.6. Relation to Other Missions

The ASPERA-3 instrument performs the first ENA imaging of another planet in the low energy range. No instruments with similar scientific objectives and capabilities have been or are foreseen to fly to other planets. The only similar experiment, ASPERA-C, was on-board the failed Mars - 96 mission. However the ASPERA-C did not have the ENA energy-analyzing detector NPD. The Japanese Nozomi launched to Mars in 1998 is concentrating on plasma measurements and does not include in its payload any ENA instrumentation. However, Mars Express and Nozomi are highly complementary missions. Nozomi with its comprehensive plasma payload provides the necessary local context for the remote ENA measurements from Mars Express. Two simultaneous plasma observations make it possible to distinguish spatial and temporal variations in the magnetospheric plasma. Particularly promising configurations would occur when one of the satellites is in the solar wind while the second one is in the near-Mars environment. In this case one can investigate the instantaneous response of the system against variations in the solar wind. Knowing the system's dynamical behavior one can evaluate the evolutionary effects more precisely.

2. THE INSTRUMENT

2.1 Overview

The ASPERA-3 experiment is designed for the analysis of ENAs, electrons, and ions with a complete coverage of the unit sphere. Mechanically the ASPERA-3 consists of two units, the Main Unit (MU) and the Ion Mass Analyzer (IMA) (Figure 5). The Main Unit comprises three sensors, NPI, NPD, ELS, and a digital processing unit, which all are located on a scanner. All mechanical and electrical interfaces are made through the scanner. The total mass of the instrument is 8.2 kg and the power consumption is 13.5 W. The Main unit envelope is $359 \times 393 \times 234 \text{ mm}^3$ and for IMA $255 \times 150 \times 150 \text{ mm}^3$. Figure 5 shows the instrument configuration and Figure 6 the instrument mechanical model during a vibration test.

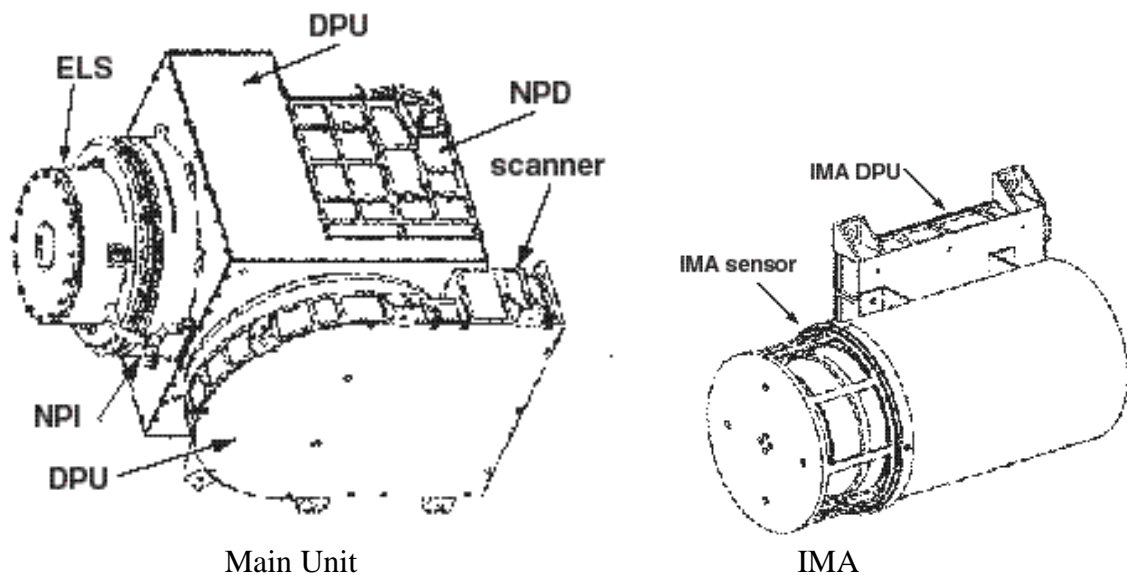


Figure 5. The ASPERA-3 configuration

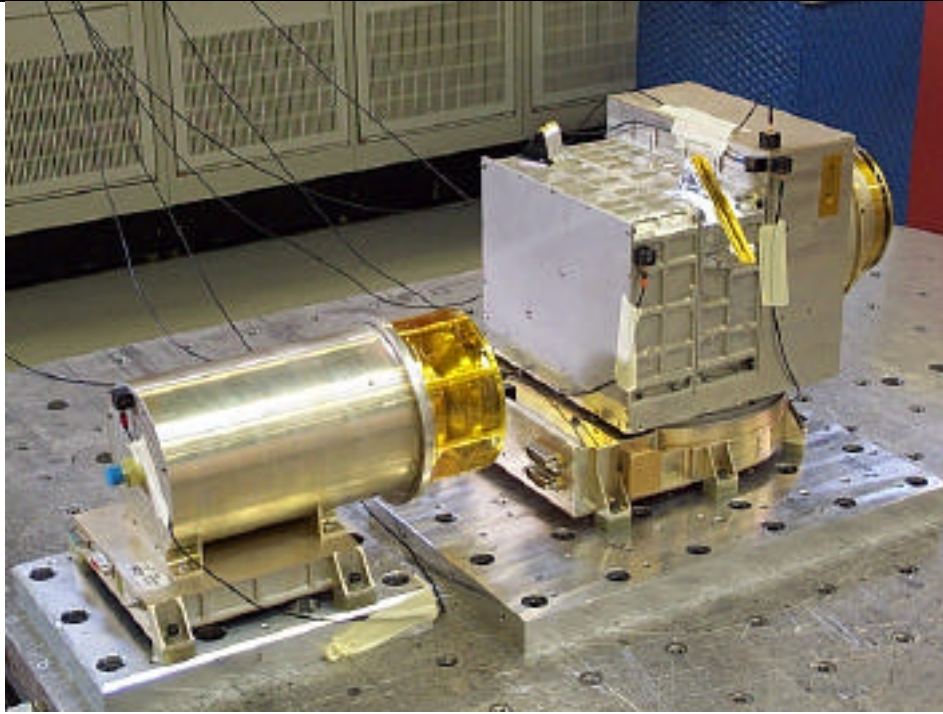


Figure 6. The ASPERA-3 instrument, IMA and the Main Unit during a vibration test.

2.2 Measurements Principles and Capabilities

To fulfill the scientific objectives listed above the ASPERA-3 instrument comprises four sensors; two ENA sensors, an electron spectrometer, and an ion mass analyzer. The two ENA sensors are optimized for some of the scientific objectives while at the same time complementing each other. This approach also gives the necessary redundancy as well as independent cross-checking, necessary for such a "first ever" measurements at another planet (there is also IMAGE/LENA which does similar measurements at Earth). The charged particle sensors not only provide characterization of the local plasma environment but also support ENA measurements in terms of charged particles background and inter - calibrations.

The Neutral Particle Imager (NPI) provides measurements of the integral ENA flux with no mass and energy resolution but with $5^\circ \times 11^\circ$ angular resolution. The intrinsic field of view is $9^\circ \times 344^\circ$. The sensor utilizes a graphite surface to suppress the UV background. ENAs incident on the surface at a grazing angle of 20° are reflected and/or cause ion sputtering. An MCP stack detects the reflected particles and sputtered fragments with a discrete anode. The NPI head is a replica of the NPI-MCP sensor developed for the ASPERA - C experiment on the Mars-96 mission (launch failure) and successfully flown on the Swedish microsatellite Astrid launched in 1995 [*C:son Brandt et al.*, 2000].

The Neutral Particle Detector (NPD) provides measurements of the ENA differential flux over the energy range 100 eV - 10 keV resolving H and O with a coarse $5^\circ \times 30^\circ$ angular resolution. The sensor consists of two identical detectors each with a $9^\circ \times 90^\circ$ intrinsic field of view. The measurement technique is based on a principle similar to NPI. ENAs incident on a surface at a grazing angle of 15° are reflected and cause secondary electron emission. The secondary electrons are transported to an MCP assembly, which gives the START signal. The reflected ENAs hit the second surface and again produce the secondary electrons used to generate the STOP signal. The time-of-flight (TOF) electronics give the ENA velocity. The pulse - height distribution analysis of the STOP signals is used to provide a rough determination of the ENA mass.

The ELectron Spectrometer (ELS) provides electron measurements in the energy range 0.01 - 20 keV. The intrinsic field of view is $10^\circ \times 360^\circ$. The 360° aperture is divided into 16 sectors. The sensor is a standard top - hat electrostatic analyzer in a very compact design. ELS is a reduced version of the MEDUSA experiment for the Astrid-2 and Munin missions launched in 1998 and 2000 [*Norberg et al.*, 2001].

The Ion Mass Analyzer (IMA), an improved version of the ion mass spectrographs TICS / Freja, IMIS/Mars-96, IMI/Planet-B [*Norberg et al.*, 1998], and an exact copy of the ICA instrument to be flown on the Rosetta mission. In this design option the IMA sensor is a separate unit connected by a cable to the ASPERA-3 experiment. IMA provides ion measurements in the energy range 0.01 - 40

keV/q for the main ion components H^+ , H_2^+ , He^+ , O^+ , and for the group of molecular ions $20 < M/q < \sim 80$. Mechanically, the IMA is a separate unit with a $4.6^\circ \times 360^\circ$ field of view. Electrostatic sweeping performs elevation ($\pm 45^\circ$) coverage. The IMA sensor is a spherical electrostatic analyzer followed by a circular magnetic separating section. A large diameter MCP with a discrete anode images the matrix azimuth \times mass.

The three sensors (NPI, NPD, and ELS) are located on a scanning platform. The combination of the 360° field of view and the scans from 0° to 180° give the required 4 maximum coverage. The real coverage depends on the instrument location on the spacecraft. Table 2 summarizes the instrument performance.

Table 2 The baseline performance of the NPI, NPD, ELS, and IMA sensors

Parameter	NPI	NPD	ELS	IMA
Particles to be measured	ENA	ENA	Electrons	Ions
Energy range, keV per charge	0.1 - 60	0.1 - 10	0.01 - 20	0.01 - 40
Energy resolution, $\Delta E/E$	No	0.8	0.07	0.07
Mass resolution,	No	H, O	N/A	No
Intrinsic field of view	$9^\circ \times 344^\circ$	$9^\circ \times 180^\circ$	$10^\circ \times 360^\circ$	$90^\circ \times 360^\circ$
Angular resolution (FWHM)	$4.6^\circ \times 11.5^\circ$	$5^\circ \times 30^\circ$	$10^\circ \times 22.5^\circ$	$4.5^\circ \times 22.5^\circ$
G-factor / pixel, cm^2sr	2.5×10^{-3} (not incl.)	6.2×10^{-3} (not incl.)	7×10^{-5}	3.5×10^{-4}
Efficiency, %, %	~ 1	1-50	Inc. in G	Inc. in G
Time resolution (full 3D), s	32	32	32	32
Mass, kg	0.7	1.3	0.3	2.2
Power, W	0.8	1.5	0.6	3.5

2.2 Neutral Particle Imager (NPI)

The NPI (Neutral Particle Imager) head is a replica of the NPI - MCP sensor developed for the ASPERA - C experiment on the Mars - 96 mission and successfully was flown on the Swedish microsatellite Astrid launched in 1995 [Barabash, 1995b].

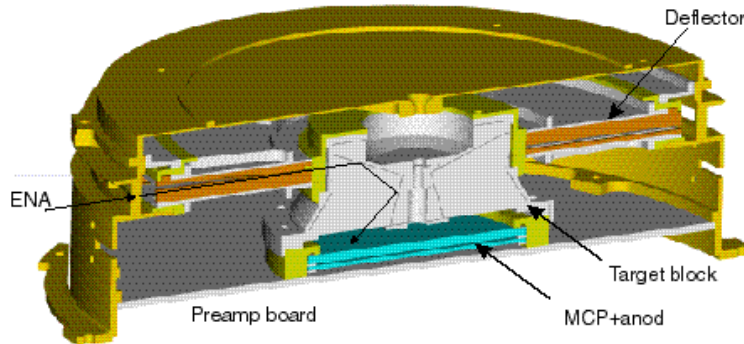


Figure 7. Cut-away view of the NPI sensor

In the NPI the charged particles, electrons and ions, are removed by the electrostatic deflection system, which consists of two disks separated by a 3 mm gap (Figures 7). The 5 kV potential between the grounded and biased disks results in a strong electric field, which sweeps away all charged particles with energies up to 60 keV. Since the integral ENA flux substantially exceeds the charged particle flux for energies greater than 60 keV, this rejection energy is sufficient for satisfactory performance. The disks also collimate the incoming beam in the elevation angle. Apart from being ON or OFF, the deflection system can be operated in two other modes, alternative mode and sweeping mode. In the alternative mode, the deflection system is turned on and off for one sampling time. This mode will be used for more accurate separation between charged and neutral particles entering the system. The deflection system is connected to the high voltage supply via an optocoupler. Regulating the optocoupler reference voltage one can change the deflection voltage performing the sweeping and

alternating. In order to reduce the time for discharging of the deflection system disks down to 1 ms, a second parallel optocoupler is used.

The space between the deflection system disks is divided into 32 sectors by plastic spokes forming 32 azimuthal collimators with an aperture of $9^\circ \times 18^\circ$ each. Neutrals passing through the deflection system hit a 32 sided cone target at a grazing angle of incidence of 20° . The interaction with the target results in secondary particle production, both electrons and ions, and/or reflection of the primary neutrals. An MCP stack in chevron configuration followed by a 32 sector anode detects the particles leaving the target. The signal from the MCP gives the direction of the primary incoming neutral. The MCP operates in ion mode with a negative bias of -2.6 kV applied to the front side and thus detects (a) sputtered positive ions of the target material, (b) positive ions resulting from ionizing of the primary neutrals, and (c) neutrals reflected from the target surface. In order to improve the angular resolution and collimate the particles leaving the interaction surface, 32 separating walls are attached to the target forming a star-like structure. This configuration allows the entering particles to experience multiple reflections and reach the MCP. NPI covers 4 in one instrument scan and produces an image of the ENA distribution in the form of an azimuth \times elevation matrix. The direction vector of 32 elements is read out once every 62.5 ms. Two sectors centered around the spin axis and looking toward the spacecraft body are blocked to provide monitoring of the MCP assembly dark counts. This space is also used for the ELS sensor harness.

An important issue in the NPI design is the coating on the target for suppressing UV photon fluxes, which enter the instrument and produce the UV background in the measurements. NPI uses the same coating as in the PIPPI and ASPERA-C experiments, namely, DAG 213, a resin-based graphite dispersion. This is similar to Aquadag, which is a graphite dispersion in water. The coating demonstrated satisfactory performance in the PIPPI experiment flown in the Earth's magnetosphere [C:son Brandt et al., 2000]. Figure 8 shows ENA images expected from NPI for four locations along the Mars Express orbit specified in Figure 2. The images were generated assuming the instrument characteristics given in Table 2. The Sun is in the center of the image. The solar wind ENAs coming from the Sun direction are not shown.

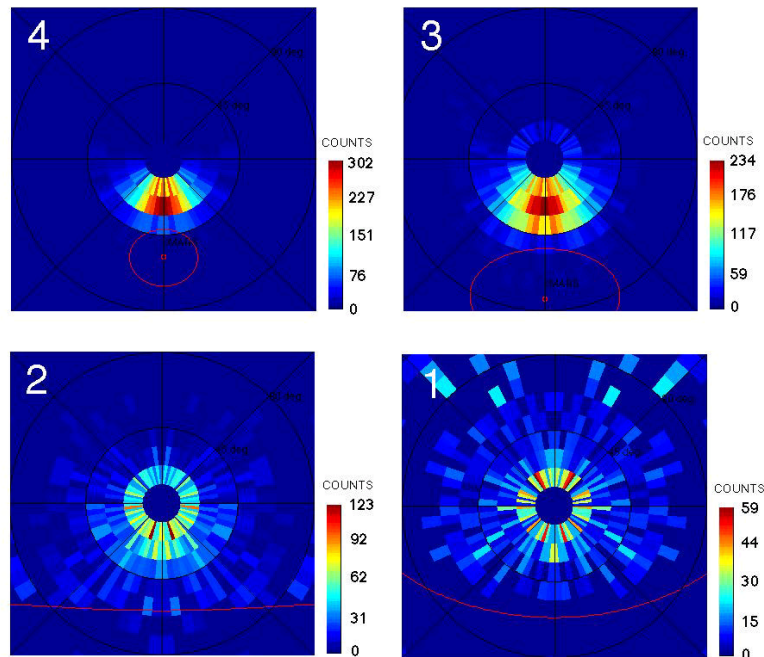


Figure 8. ENA images expected from NPI for four locations along the Mars Express orbit specified in Figure 2. The images were generated assuming the instrument characteristics given in Table 2. The projection is similar to Figure 3.

2.3 Neutral Particle Detector (NPD)

The NPD sensor consists of two identical detectors, each of which is a pinhole camera. Figure 9 provides a conceptual view of one detector.

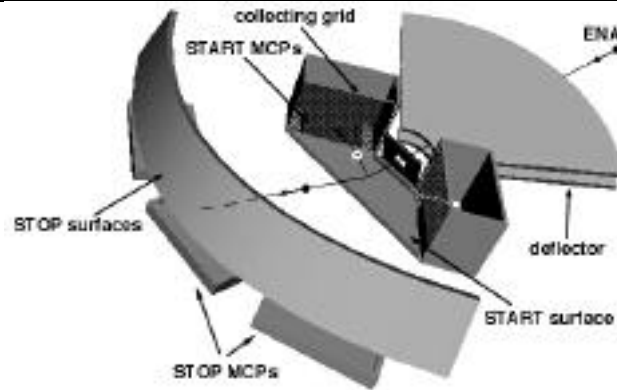


Figure 9. Three-dimensional view of the NPD principal components

In each detector the charged particles, electrons and ions, are removed by the deflection system, which consists of two 90° sectors separated by a 4.5 mm gap. In the normal operational mode the 10 kV potential (± 5 kV) applied to the disks and the resulting strong electric field sweeps away all charged particles with energies up to 70 keV. The deflector also collimates the incoming beam in the elevation angle. The collimated ENA beam emerging from the 3.5×4.5 mm pin-hole hits the START surface under the 15° grazing angle and causes a secondary electron emission. By a system of collecting grids, the secondary electrons (SE) are transported to one of two MCP assemblies giving the START signal for TOF electronics.

Depending on the azimuth angle, the collection efficiency varies from 80% to 95%. The incident ENAs are reflected from the START surface near-specularly. Since the charge state equilibrium is established during the interaction with the surface, the emerging beam contains both the neutral and ionized (positive and negative) components. To increase the total efficiency, no further separation by the charge is made. As proven by the ion tracing, there is very little disturbance to the reflected atomic ions leaving the START surface with an energy above 80 eV, introduced by the START electron optics. Figure 10 shows the results of electron and ion ray-tracing in the START assembly electron optic.

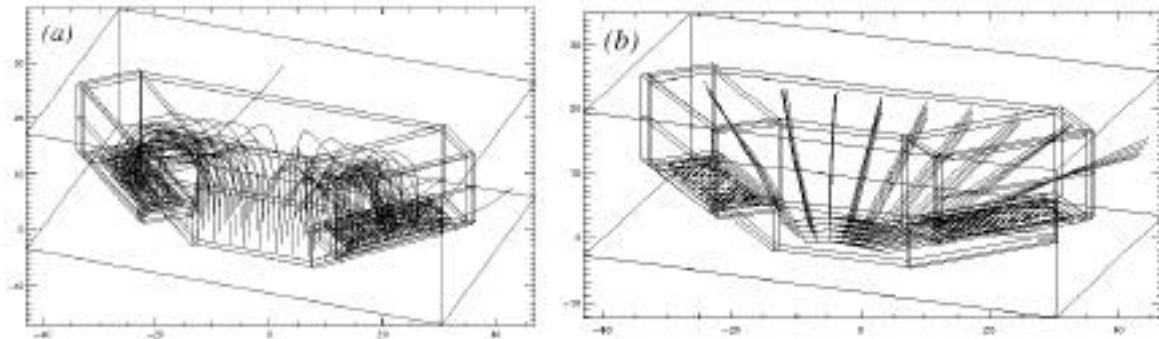


Figure 10. The ray-tracing of the electron (a) and 80 eV ion trajectories (b) in the START assembly electron optics.

Therefore particles of all charge states - negative, neutral, and positive - will impact the second surface, the STOP surface, and again produce secondary electrons, which are detected by one of the three MCP assemblies giving the STOP signal. The time of flight over a fixed distance of 8 cm defines the particle velocity. The STOP MCPs also give the azimuthal direction. Since the SE yield depends on mass for the same velocity, the pulse height distribution analysis of the STOP signals provides the estimation of ENA mass. Each event is stored in the array STOP MCP charge \times time-of-flight \times direction. The array is accumulated over the sampling time 62.5 μ s. Figure 11 shows the technological model of the NPD sensor.



Figure 11. Technological model of the NPD sensor

The selection of the START and STOP surfaces is the most difficult part of the NPD development. Extensive studies have been performed at University of Bern [Jans, 2000] and Brigham Young University (USA) to optimize the performance of the surfaces which must satisfy a number of requirements, namely, high secondary electron yield, high UV absorption even at grazing angles, high particle reflection coefficient (START surface), low angular scattering of ions, low photoelectron yield. For the START surface we chose a multi-layer coating composed of a thin layer of Cr_2O_3 , covered by a thicker layer of MgF , and topped with a thin layer of WO_2 . The coating is optimized for the absorption of the 121.4 nm line at the 15° incident angle. The reflection coefficient reached was about 30%, a factor of 2 lower than the uncoated surface. The coating is applied on a titanium substrate polished down to 100\AA roughness.

The STOP surface is graphite (roughness around 100 nm) covered by a MgO layer of about 500 nm.. This combination has a very high secondary electron yield, low photoelectron yield and high UV absorption. A lot of efforts have been made to increase the stability of the MgO coating against moisture. It was established that polishing the graphite substantially improves the stability and possible increases in air humidity during storage and pre-launch operations does not present any problems for the surface performance. Therefore, both surfaces are stable and do not require special maintaining. Figure 12 presents the expected count rates for different ENA and UV fluxes (Lyman-) and a TOF window of 1.56 ms defined by the slowest (300 eV) oxygen atoms travelling the time-of-flight distance. The valid count rates are given for different species and energies because the secondary electron yield and reflection coefficient variations. We take an energy window of 1 keV and assume the coefficients describing the interaction with the surface to be constant. In reality, of course, the instrument measures over the entire energy range 0.1 - 10 keV. Therefore, Figure 12 gives count rates for a narrow (in energy sense) beam of the oxygen and hydrogen atoms. The expected UV flux is about 4 kR close to the Martian limb [Anderson, 1974] that gives a count rate (signal-to-noise-ratio is the unit) equal to $2 \cdot 10^5 \text{ cm}^{-2} \text{ s}^{-1} \text{ sr}^{-1} \text{ keV}^{-1}$ (H, 140 eV), $3 \cdot 10^4 \text{ cm}^{-2} \text{ s}^{-1} \text{ sr}^{-1} \text{ eV}^{-1}$ (H, O , few keV), and $4 \cdot 10^3 \text{ cm}^{-2} \text{ s}^{-1} \text{ sr}^{-1} \text{ eV}^{-1}$ (O, 10 keV).

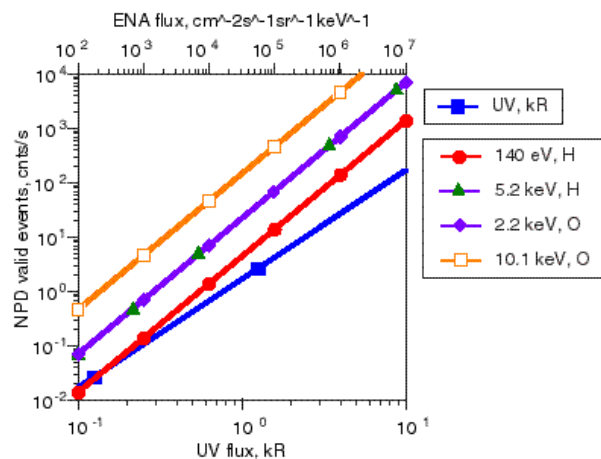


Figure 12. The UV (Lyman-) background and valid ENA count rates expected for different energies and species for an 1 keV energy window.

The initial tests with the NPD technological model gave results fully corresponding to the specified performance. Figure 13 shows TOF spectra for 2 keV beams of different masses.

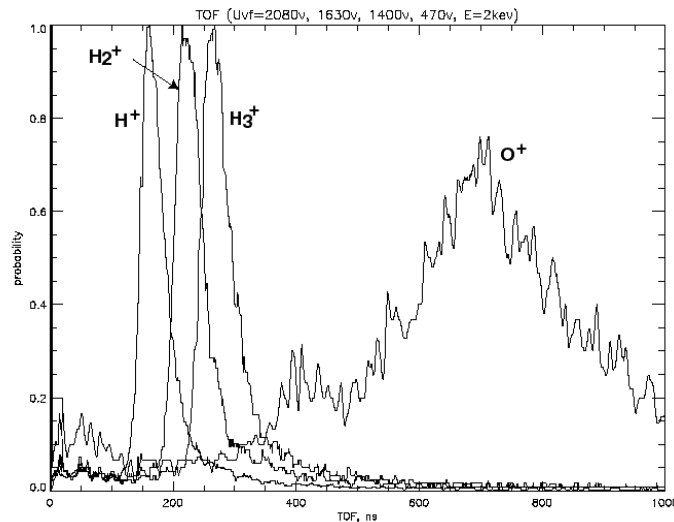


Figure 13. NPD TOF spectra for 2 keV beams of different masses.

Figure 14 summarizes TOF measurements. The dashed lines show the theoretical dependence corresponding to the 34% energy loss in the START surface.

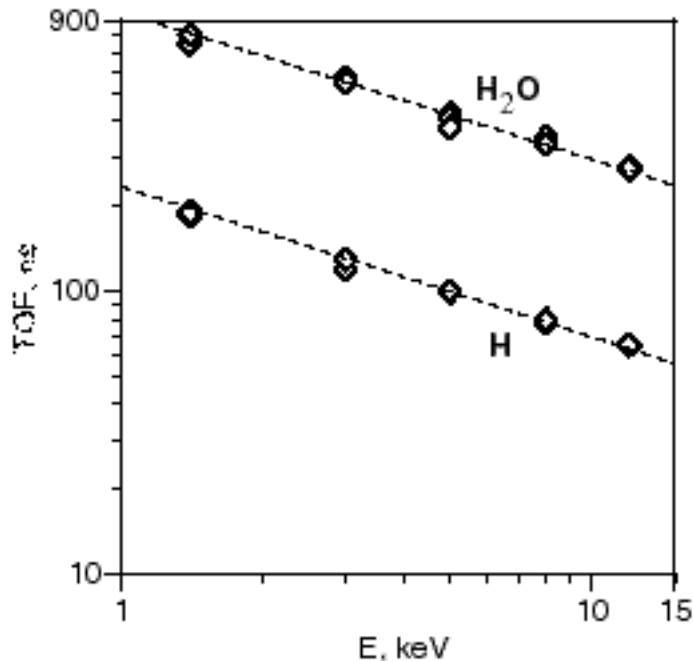


Figure 14. The time-of-flight measurements for different masses as a function of energy. The dashed lines give the theoretical dependence corresponding to the 34% energy loss.

The water molecules produced in the ion source break-up during the impact but the residual components carry the same initial velocity corrected for the energy loss in the target. This figure shows that within the range 1 – 10 keV the time-of-flight measurements give reliable mass identification. The other independent way of mass identification is based on the dependence of the amount of electrons produced from the STOP surface on mass. Figure 15 shows a pulse-height distribution of the valid (START-STOP) signals obtained from the STOP MCP when a beam of 15 keV H_2O^+ ions was used. The different peaks correspond to different amounts of secondary electrons released from the STOP surface.

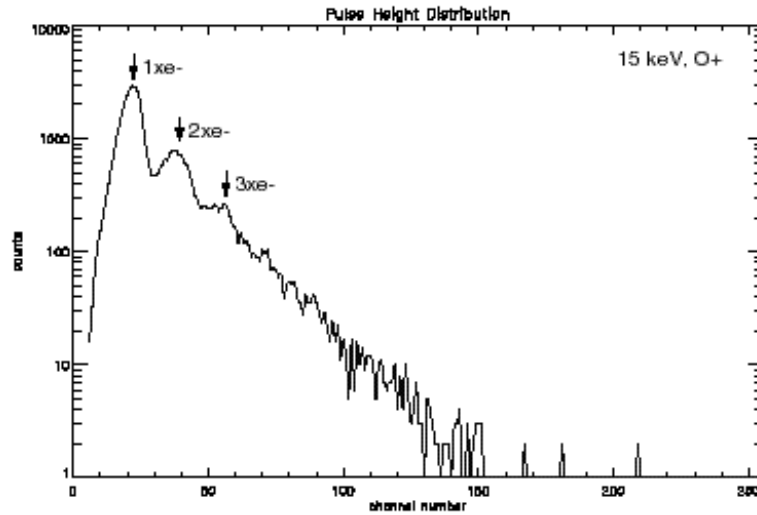


Figure 15. Pulse–height distribution of the valid (START-STOP) signals obtained from the STOP MCP under a beam of 15 keV H_2O^+ ions.

2.4 Electron Spectrometer (ELS)

The Electron Spectrometer (ELS) sensor represents a new generation of ultra-light, low-power, electron sensor (Figure 16). It is formed by a spherical top-hat electrostatic analyzer and a collimator system. Particles enter the aperture at any angle in the plane of incidence. Electrons are then deflected into the spectrometer by applying a positive voltage to the inner spherical electron deflection plate. The electrons hit a micro channel plate (MCP) after being filtered in energy by the analyzer plates. The plates are stepped in voltage to achieve an energy spectrum.

Electrons with energies up to 20 keV/q will be measured, with a maximum time resolution of one energy sweep per four seconds. There are 16 anodes behind the MCP, each anode defining a 22.5° sector and each connected to a preamplifier. The ELS sensor will be mounted on the ASPERA-3 scan platform, on top of the NPI sensor, in such a way that the full 4° angular distribution of electrons will be measured during each platform scan.

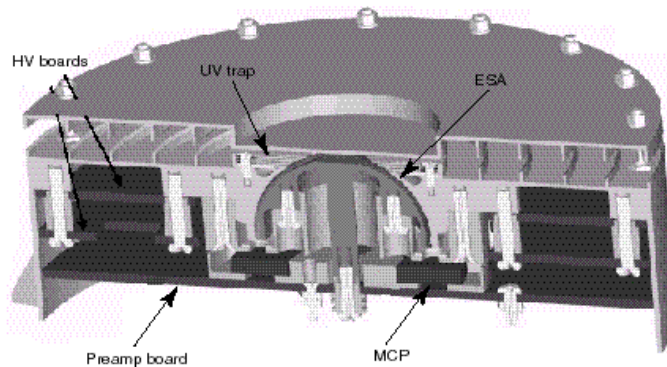


Figure 16. Cut-away view of the ELS sensor

2.5 Ion Mass Analyzer (IMA)

The Ion Mass Analyzer (Figure 17) is an improved version of the ion mass spectrographs TICS (Freja, 1992), IMIS (part of ASPERA-C, Mars-96, 1996), and IMI (Planet-B, 1998) [Norberg *et al.*, 1998]. It is an exact copy of the ICA instrument to be flown on Rosetta to comet Wirtanen in 2003. Particles enter the analyzer through an outer grid. Behind the grid is a deflection system whose purpose is to deflect particles coming from angles lying between 45° and 135° with respect to the symmetry axis, into the electrostatic analyzer (ESA). Ions within a swept energy pass band will pass the ESA. The ions are then deflected in a cylindrical magnetic field set up by permanent magnets. The field deflects lighter ions more than heavy ions away from the center of the analyzer. The ions finally hit a micro-channel plate (MCP) and are detected by an anode system. Ions are simultaneously

analyzed regarding both direction and mass per charge. The magnet assembly can be biased with respect to the ESA to post-accelerate ions. This post-acceleration enables a selection of both mass range and mass resolution (Figure 17).

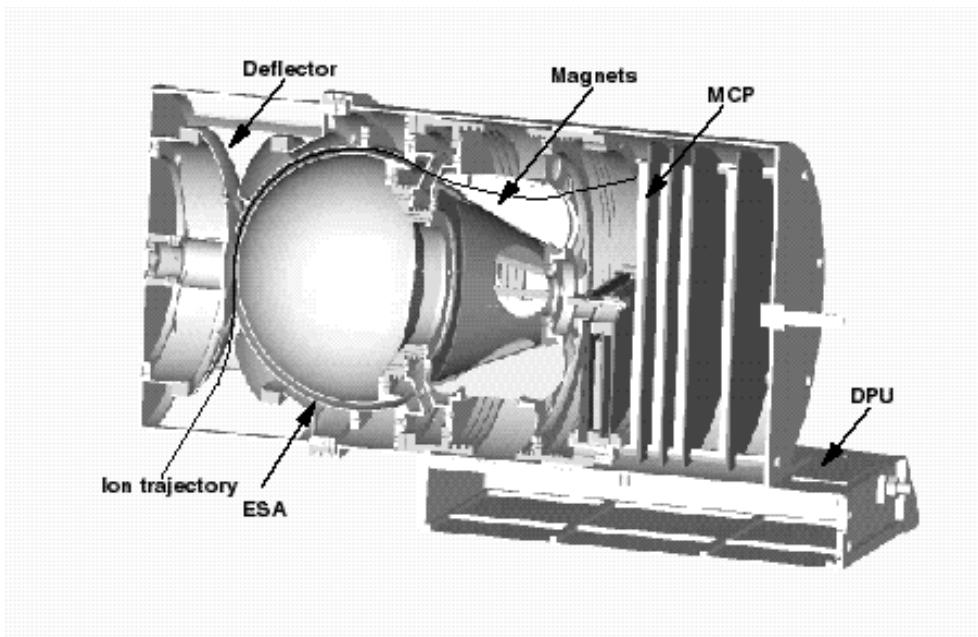


Figure 17. Cross-away view of the IMA sensor.

The electrons from the MCP are detected by an "imaging" anode system. A system of 32 concentric rings behind the MCP measures the radial impact position (representing ion mass), whereas 16 sector anodes measure the azimuthal impact position (representing ion entrance angle). The read-out system is based on discrete pre-amplifiers. Six MOCAD chips provide 48 independent channels, 32 rings and 16 sectors. Each chip contains 8 channels including a charge-sensitive preamplifier, shaper and a discriminator. The TTL outputs are fed to an FPGA device for decoding, addressing, and coincidence analysis. Figure 18 demonstrates the achieved mass resolution at 6 keV ion energy.

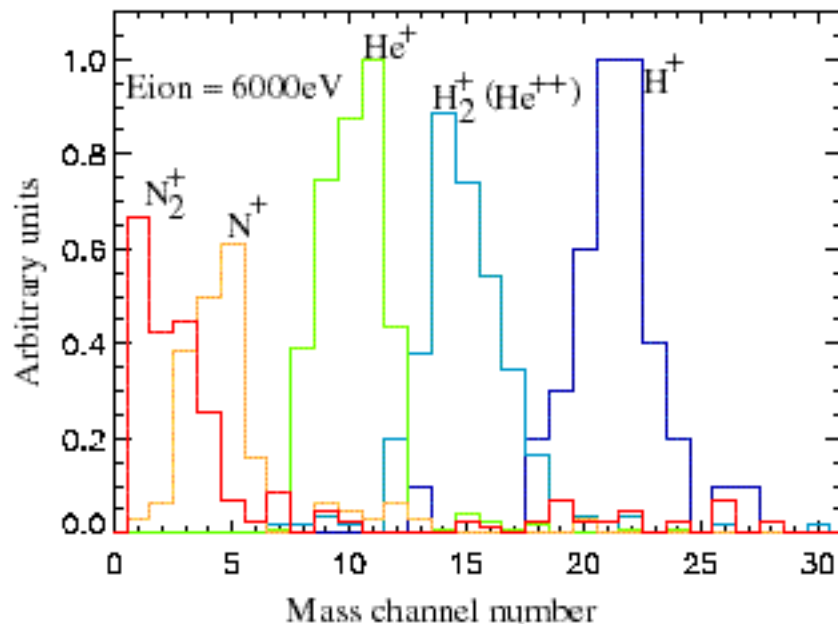


Figure 18. IMA mass resolution at 6 keV energy.

3. THE TEAM

The ASPERA-3 experiment is a large consortium including 15 groups from 10 countries over the entire Europe, USA, and Japan. Table 3 shows the primary hardware responsibilities for the different groups.

Table 3. ASPERA-3 groups and primary hardware responsibilities.

Organization	Primary contribution
Swedish Institute of Space Physics, Kiruna, Sweden	PI-institute, NPI, NPD, IMA, scanner
Institute of Space and Astronautical Science, Sagamichara, Japan	Collaboration with Nozomi, NPI calibrations
University of Bern, Physikalisches Institut, Switzerland	NPD surfaces, NPD mechanics
Instituto di Fisica dello Spazio Interplanetari, Rome, Italy	EGSE, NPI mechanics, NPD electronics
Mullard Space Science Laboratory, UK	ELS calibrations
University of Arizona , Tucson, USA	START surface, NPD UV calibrations
Space Research Institute, Moscow, Russia	NPD design
Southwest Research Institute , San Antonio	ELS, IMA imaging detector
Rutherford Appleton Laboratory , Oxfordshire, UK	NPD MCPs
Finnish Meteorological Institute, Helsinki, Finland	DPU, theory
Space Physics Research Laboratory /University of Michigan, Ann Arbor, USA	Theory
Max-Planck-Institut für Aeronomie, Katlenburg-Lindau, Germany	NPD electronics
Space Science Laboratory /University of California in Berkeley, Berkeley, USA	Theory
Space technology Ltd., National University of Ireland, Ireland	Hardware support
Applied Physics Laboratory/John Hopkins University , Laurel, USA	Theory
Centre d'Etude Spatiale des Rayonnements, Toulouse, France	NPI MCPs, IMA calibrations, DC/DC board, scanner drivers

4. REFERENCES

- Acuna, M. H., et al., Magnetic Field and Plasma Observations at Mars: Initial Results of the Mars Global Surveyor mission, *Science*, 279, 1676, 1998.
- Anderson, D. E., Mariner 6, 7, and 9 ultraviolet spectrometer: Analysis of hydrogen Lyman alpha data, *J. Geophys. Res.*, 79, 1513-1518, 1974.
- Barabash, S., et al., Diagnostic of energetic neutral particles at Mars by the ASPERA-C instrument for the Mars 96 mission, *Adv. Space Res.*, 16, (4)81, 1995a.
- Barabash, S., Satellite observations of the plasma - neutral coupling near Mars and the earth, *IRF Scientific Report*, 228, 1995b.
- Barabash, S., M. Holmström, A. Lukyanov, and E. Kallio, Energetic neutral atoms at Mars IV: Imaging of planetary oxygen, submitted to *J. Geophys. Res.*, 2001.
- Brecht, S.H., Solar Wind proton deposition into the Martian atmosphere, *J. Geophys. Res.* 102, 11,287, 1997.
- C:son Brandt, P., S. Barabash, G. R. Wilson, E. C. Roelof, C. J. Chase, Energetic neutral atom imaging at low (< 10 keV) energies from Astrid: Observations and simulations, *J. of Atmos. and Solar Terrestrial Phys.*, 62, 901-910, 2000.
- Dornheim, M. A., Mars atmosphere thicker than expected, *Aviation Week and Technology*, September 29, 36, 1997,
- Dubinin, E., et al., Plasma characteristics of the boundary layer in the Martian magnetosphere, *J. Geophys. Res.*, 101, 27,061, 1996.
- Holmström, M., S. Barabash, E. Kallio, Energetic neutral atoms at Mars I: Imaging of solar wind protons, submitted to *J. Geophys. Res.*, 2001.
- Jans, S., Ionization of energetic neutral atoms for application in space instrumentation, Diplomarbeit der Philosophisch-naturwissenschaftlichen Fakultät der Universität Bern, 2000.
- Farmer, C. B., et al., Mars: Water vapour observations from the Viking orbiters, *J. Geophys. Res.*, 82, 4225, 1977.
- Kallio, E., J. G. Luhmann, and S. Barabash, Charge exchange near Mars: The solar wind absorption and energetic neutral atom production, *J. Geophys. Res.* 102, 22,183, 1997.
- Kallio, E., and H. Koskinen, A test particle simulation of the motion of oxygen ions and solar wind protons near Mars, *J. Geophys. Res.*, 104, 557-579, 1999.
- Kallio, E. and P. Janhunen, Atmospheric effects of proton precipitation in the Martian atmosphere and its connection to the Mars-solar wind interaction, *J. Geophys. Res.*, 106, 5617, 2001.
- Kallio, E., and S. Barabash, On the elastic and inelastic collisions between the precipitating energetic hydrogen atoms and the Martian atmospheric neutrals, *J. Geophys. Res.*, 105, 24973-24996, 2000.
- Kallio, E., and S. Barabash, Atmospheric effects of precipitating energetic hydrogen atoms to the Martian atmosphere, *J. Geophys. Res.*, 106, 165-177, 2001.
- Lichtenegger, H., H. Lammer, W. Stumptner, Energetic neutral atoms at Mars III: Flux and energy distribution of planetary energetic H atoms, submitted to *J. Geophys. Res.*, 2001.
- Luhmann, J. G. and J. U. Kozyra, Dayside pickup oxygen ion precipitation at Venus and Mars: Spatial distributions, energy deposition and consequences, *J. Geophys. Res.*, 96, 5457, 1991.

- Luhmann, J. G., et al., Evolutionary impact of sputtering of the Martian atmosphere by O⁺ pickup ions, *Geophys. Res. Lett.*, 19, 2151, 1992.
- Luhmann, J. G., and S. J. Bauer, Solar wind effects on atmospheric evolution at Venus and Mars, in *Venus and Mars: Atmospheres, ionospheres, and solar wind interactions*, AGU monograph, 66, 417-430, 1992.
- Lundin, R., et al., First measurements of the ionospheric plasma escape from Mars, *Nature*, 341, 609, 1989.
- Lundin, R., et al., On the momentum transfer of the solar wind to the Martian topside ionosphere, *Geophys. Res. Lett.* 18, 1059, 1991.
- Lundin, R., et al., ASPERA observations of Martian magnetospheric boundaries, in *Plasma environments of non-magnetic planets*, ed. by T. I. Gombosi, Pergamon Press, p. 311, 1993.
- McKay, C. P., and C. R. Stoker, The early environment and its evolution on Mars: implications for life, *Rev. of Geophys.*, 27, 189, 1989.
- Mura, A., A. Milillo, S. Orsini, E. Kallio, S. Barabash, Energetic neutral atoms at Mars II: Energetic Neutral Atom production near Phobos, submitted to *J. Geophys. Res.*, 2001.
- Norberg, O., M. Yamauchi, R. Lundin, S. Olsen, H. Borg, S. Barabash, M. Hirahara, T. Mukai, and H. Hayakawa, The Ion Mass Imager on the Planet-B spacecraft, *Earth, Planets, and Space*, 50, 199-205, 1998.
- Norberg O., J. D. Winningham, H. Lauche, W. Keith, W. Puccio, J. Olsen, K. Lundin, and J. Scherrer, The MEDUSA electron and ion spectrometer and the PIA ultraviolet photometers on Astrid-2, *Ann. Geophys.*, 19, 593, 2001.
- Perez-de-Tejada, H., Solar wind erosion of the Mars early atmosphere, *J. Geophys. Res.*, 97, 3159, 1992.
- Roelof, E. C., and A. J. Skinner, Extraction of ion distributions from magnetospheric and EUV images, *Space Sci. Rev.*, 91, 437-459, 2000.
- Verigin, M., et al., On the problem of the Martian atmosphere dissipation: PHOBOS 2 TAUS spectrometer results, *J. Geophys. Res.*, 96, 19,315 - 19,320, 1991.
- Wurz, P., Detection of Energetic Neutral Particles, in *The Outer Heliosphere: Beyond the Planets*, (eds. K. Scherer, H. Fichtner, and E. Marsch), Copernicus Gesellschaft, Katlenburg-Lindau, Germany, 251-288, 2000.